Time-Frequency Analysis of Functional Optical Mammographic Images

Randall L. Barbour,[1,2] Harry L. Graber,[1] Christoph H. Schmitz,[1] Frank Tarantini,[3] Georges Khoury,[3] David J. Naar,[3] Thomas F. Panetta,[3] Theophilus Lewis,[4] and Yaling Pei[2]

Departments of [1]Pathology and [4]Surgery, SUNY Downstate Medical Center,
450 Clarkson Avenue, Brooklyn, NY 11203 USA

[2]NIRx Medical Technologies, LLC, 15 Cherry Lane, Glen Head, NY 11545 USA

[3]Department of Vascular Surgery, Staten Island University Hospital, Staten Island, NY 10305 USA

ABSTRACT

We have introduced working technology that provides for time-series imaging of the hemoglobin signal in large tissue structures. In this study we have explored our ability to detect aberrant time-frequency responses of breast vasculature in subjects with Stage II breast cancer, at rest and in response to simple provocations. The hypothesis being explored is that time-series imaging will be sensitive to the known structural and functional malformations of the tumor vasculature. Mammographic studies were conducted using an adjustable hemispheric measuring head containing 21 source and 21 detector locations (for 441 source-detector channels). Simultaneous dual-wavelength (760 and 830 nm) studies were performed on women lying prone with the breast hanging in a pendant position. Two classes of measure were performed: 1) 20-minute baseline measurements wherein the subject was at rest; 2) provocation studies wherein the subject was asked to perform some simple breathing maneuvers. Collected data were analyzed to identify the central tendencies and time-frequency structure of the detector responses, and those of the image time series. Image data were generated using the Normalized Difference Method [Pei *et al*., *Appl. Opt.* **40**, 5755-5769 (2001)]. Results obtained clearly document three classes of dynamic anomaly in the tumor-bearing breast relative to the healthy contralateral breast. First, breast tumors exhibit oxygen supply/demand imbalance in response to an oxidative challenge (breath hold). Second, the vasomotor response of the tumor vasculature is mainly depressed and exhibits an altered modulation. Third, the region of the breast wherein the altered vasomotor signature is seen extends well beyond the margins of the tumor itself.

1. INTRODUCTION

Maintenance of physiological homeostasis is critically dependent on the functionality of the vasculature. Delivery of essential nutrients, removal of metabolic wastes, trafficking of hormonal signals, modulation of immune responses, and temperature regulation are but a few of the critical roles played by the vasculature. In addition, it is well appreciated that the vascular response is controlled by both local and systemic effectors. Although much is known regarding these effectors and their control mechanisms, the details of their actions on a local level and their coordinated system-wide actions are known only in the grossest of ways. Recently we have put forward the hypothesis that near infrared (NIR) optical tomography is a viable approach to studying the dynamics of vascular beds in large tissue structures without the need for contrast agents [1]. The rationale for this hypothesis is the simple observation that hemoglobin, which is ordinarily confined to the vascular space, can be monitored noninvasively and continuously at NIR wavelengths. It follows that time-dependent variations in the hemoglobin signal can be taken as a reliable measure of vascular reactivity reflecting local changes in tissue blood volume. In addition, because hemoglobin is the principal oxygen carrier molecule in the blood and has distinct oxygen-sensitive absorption spectra, such measures can also reveal variations in tissue oxygen supply/demand. We believe that the ability to simultaneously explore vascular reactivity and local metabolic demand has enormous potential to provide for fundamental strides in attaining new insights into basic physiological processes, as well as for developing new approaches to disease detection, disease prognosis, and guiding of therapy. To this end we have undertaken a technology development effort intended to provide a practical measuring system that is capable of exploring the details of the dynamics of the vascular bed [2-4]. The result of this effort has been the development of a real-time imaging system known as DYNOT (for **dy**namic **n**ear infrared **o**ptical **t**omography) [2], which we are currently evaluating in order to determine its practical utility. In this report we present results from

preliminary studies in which we have used DYNOT to explore the vascular response of solid tumors of the breast to simple maneuvers.

An important point, stressed in our first dynamic-imaging report [1] and has elaborated upon in subsequent papers and presentations [5-7], is that the most effective means of extracting clinically valuable information available from NIR optical tomography is through application of mathematical time-series analysis methods to sequences of detector data and/or reconstructed images rather than by direct inspection of individual optical coefficient or hemoglobin concentration images. This point is born out by the case results to follow, wherein a different analytic strategy we are studying was used to analyze the data collected from each subject. It should be noted that the employment of different techniques in each case also affects the structure of the current report: following a general description of the DYNOT system and data collection techniques in Instrumentation/Methods, the analysis method applied to each subject's data is described, where necessary, prior to presentation of the corresponding dynamic feature map(s), in Results.

2. INSTRUMENTATION/METHODS

The measuring system we have developed [2,4] is modular in design and can be made to fit within an instrument cart measuring 30″ W × 44″ L × 40″ H. System hardware includes time-multiplexed, frequency-encoded, multi-wavelength illumination, fast source switching (up to 90 Hz), and on-the-fly adaptive gain control (dynamic range 180 dB). These capabilities allow for continuous data collection at rates up to 10 kHz while providing full tomographic images (32 sources × 32 detectors) at a rate of ~3 Hz. Mounted to the cart are two articulating arms; one to hold the system PC controller and the other to provide facile positioning of the tomographic measuring head, of which four designs have been implemented: a folding hemisphere for breast imaging, a circular ring for limb imaging, a helmet design for brain imaging, and a planar array. The first of these, shown in Figure 1, was used for the studies reported on here. The measuring head was juxtaposed to the examination table on which the subject lay. The breast being examined hung pendant through a circular hole in the table, and the measuring head was translated and its diameter adjusted until all 21 optical fibers were in firm contact with the skin. (No subject reported any discomfort during any part of the procedure.)

Accompanying system hardware is an integrated suite of software that provides for five levels of system control and data analysis. This includes software for (1) automated instrument set-up, calibration and control, (2) real-time display of relative changes in hemoglobin levels, (3) real-time image recovery yielding a time series of 2D/3D images, (4) real-time interactive volume rendering and (5) software for linear and nonlinear time-series image analysis. A schematic of system hardware and software functionality is shown in Figure 2.
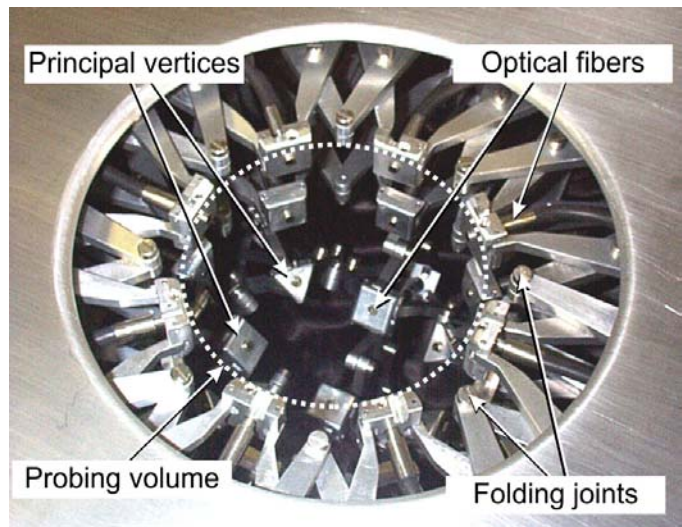
Figure 1. Photograph of hemispheric breast measuring head Diameter is adjustable over range of 4 cm to 12 cm, with all fibers normal to a hemispheric surface at all diameters.

Image reconstruction was carried out by means of the previously described Normalized Difference Method [8], augmented with more recently implemented preconditioning and weight-matrix transformation operations [9]. The solution to each inverse problem was calculated via truncated singular value decomposition, which is computationally efficient and regularizes the problem [9].

3. RESULTS

3.1 Fourier Analysis of Total Hemoglobin (i.e., Blood Volume) Time Series
To enhance possible differences in tumor perfusion from the surrounding tissue, Subject I (4 cm × 7 cm tumor) was asked to perform a series of deep breathing maneuvers all the while time series image data were being collected. This maneuver was selected because it is a simple means to modulate venous return. The expected finding is that the
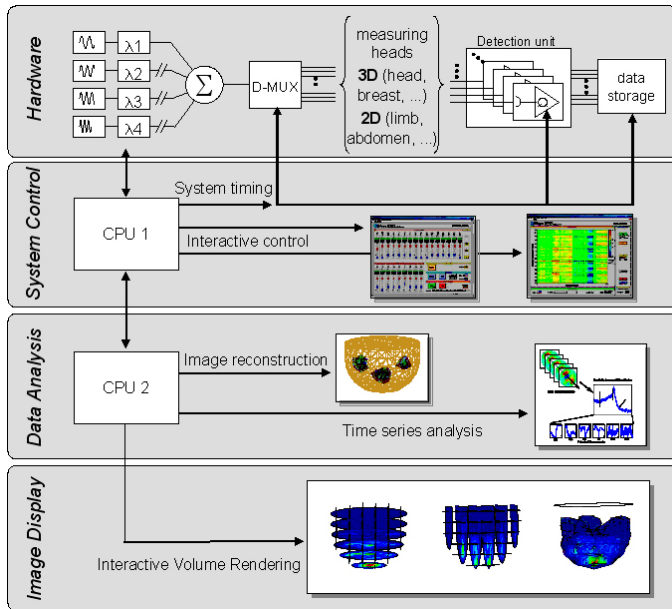
Figure 2. Functional layout of the DYNOT system. Detector data (System Control subsystem) can be visualized while they are being collected. These data also can be spooled directly to the image reconstruction software (Data Analysis subsystem), and image reconstruction, display, and post-processing operations commenced while the measurement still is in progress.

presence of a disorganized vascular bed associated with the tumor [10] will cause local delays in tissue perfusion, which can be revealed by a spatial map of the phase of the respiratory signal. The protocol for data collection and analysis was: 1) subject engaged in deep regulated breathing for one minute; 2) simultaneous dual-wavelength measurements were performed at a rate of ~3 (441-channel detector readings data sets) per second during this time; 3) time series of absorption coefficient (μ_a) images, at both wavelengths, were reconstructed; 4) a time series of spatial maps of total hemoglobin concentration (Hb-t) was computed from the μ_a images for each time point; 5) the discrete Fourier transform of the Hb-t time series in each pixel was computed; 6) a spatial map of the phase at the controlled respiratory frequency was generated.

Figure 3 shows an x-ray mammogram of the subject's breast. Present is a large infiltrating carcinoma measuring 4 cm ×7 cm, oriented from the lower medial to the upper lateral regions of the breast. Figure 4 shows the corresponding spatial map of phase recovered from the analysis of the Fourier transforms of the time-series image pixel data. For comparison purposes we also show the corresponding spatial map obtained from the contralateral non-tumor-bearing breast of the same subject, following the outlined protocol. Inspection of the phase map of the tumor-bearing breast shows that, with the exception of some surface artifacts, is a distinct region roughly following the orientation indicated in the x-ray image and having a phase notably different from the surrounding tissue is clearly present. These findings are in contrast the mainly featureless phase map obtained for the tumor-free breast, which suggests that perfusion is largely coherent in the latter breast.
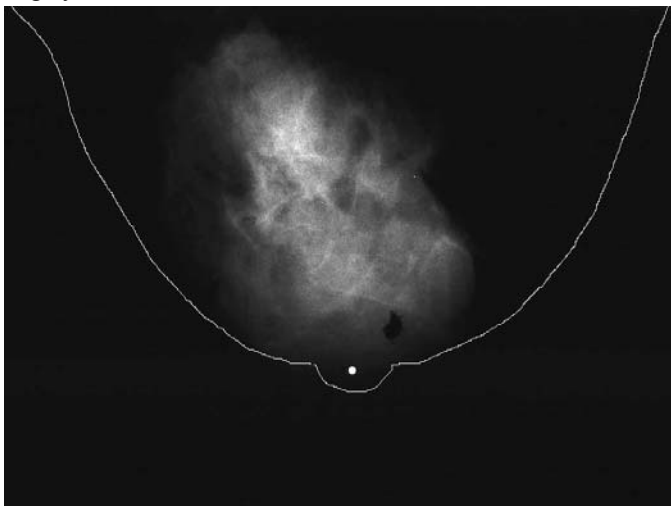

Figure 3. x–ray mammogram (craniocaudal view) of the right (tumor–bearing) breast of Subject I; external boundary of breast is indicated by the white curve.
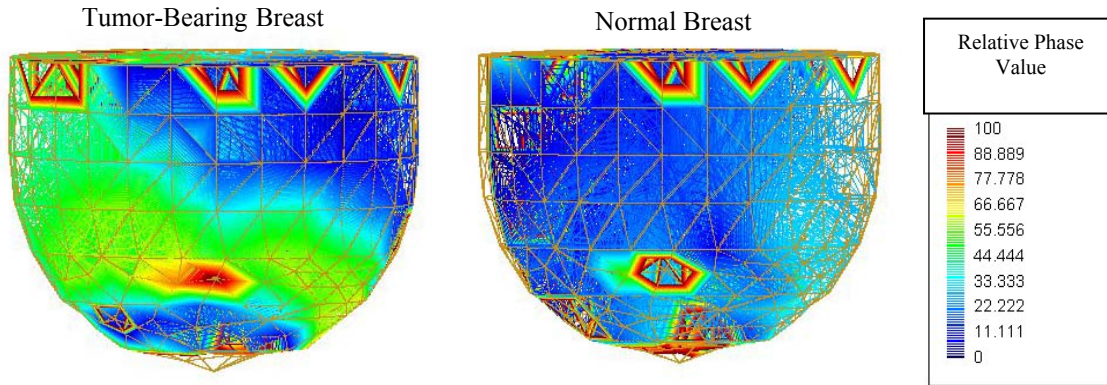
Figure 4. Spatial maps of phase at the respiratory frequency.

3.2 Temporal Derivative Analysis of Oxyhemoglobin and Deoxyhemoglobin Time Series

Subject II (2 cm diameter tumor) was asked to perform a breath-hold for a period lasting approximately one minute. The rationale for this maneuver is that the enhanced metabolic activity associated with a growing tumor, combined with a possibly compromised vascular supply, could push the tumor tissue into oxygen debt, which would cause a decline in the level of oxyhemoglobin (Hb-o) together with a rise in the level of deoxyhemoglobin (Hb-r). In Figure 5 we show a typical time course in the measured normalized levels of Hb-o and Hb-r obtained before (1 and 2), during (3) and after (4) the breath hold, for the healthy and tumor-bearing breasts. Comparison between the graphs reveals a qualitatively different trend in hemoglobin states during the breath hold. In both graphs, the Hb-o and Hb-r levels rose initially upon a breath hold, which is the expected response because the associated rise in venous return pressure will cause an increase in tissue blood volume. Following this we observed that contrary to the trend seen in the healthy breast, the Hb-o level in the tumor-bearing breast became unstable and then declined. At the same time, the Hb-r level climbed more rapidly than in the breast that did not contain a tumor. These findings are entirely consistent with the well-recognized general finding that solid tumors function on the brink of hypoxemia.
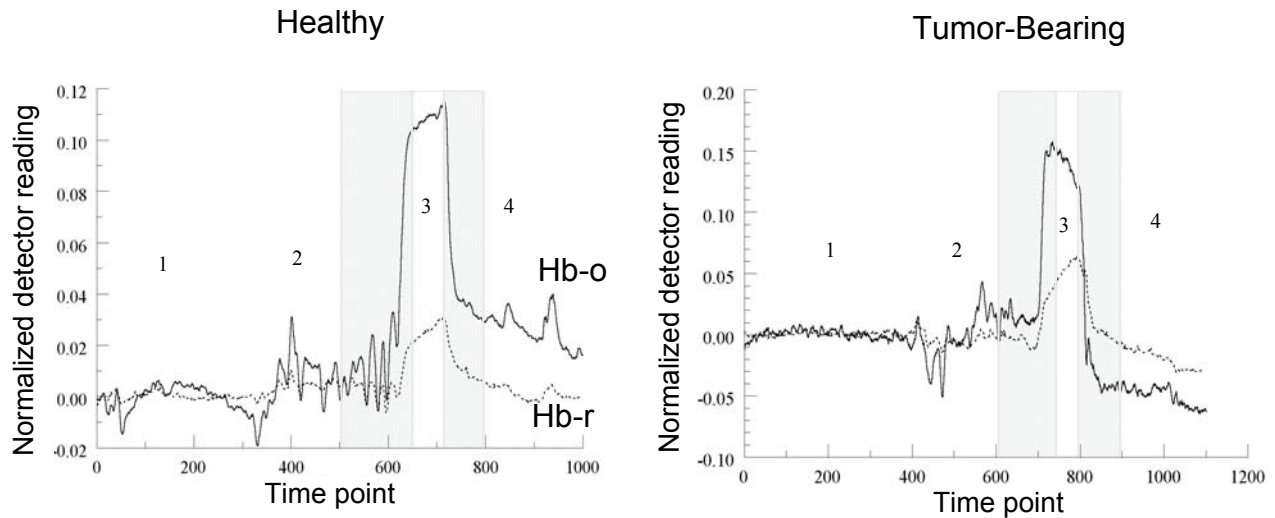

Figure 5. Hb-o and Hb-r time series computed from representative dual-wavelength detector readings, Subject II.

In Figure 6 we show an example of how information of the sort in Fig. 5, but extracted from the image time series reconstructed from the tomographic measurements, can serve to image the tumor with high contrast. The data-analysis protocol was: 1) subject held her breath for approximately one minute; 2) simultaneous dual-wavelength measurements were performed at a rate of ~3 Hz during this time; 3) time series of absorption coefficient (μ_a) images, at both wavelengths, were reconstructed; 4) time series of spatial maps of Hb-o and Hb-r were computed from the μ_a images for each time point; 5) linear regression computations were performed to determine the average rate of change of Hb-o and Hb-r in each image pixel, within time period 3 (narrow white bar within the gray bar) indicated in Fig. 5; 6) a spatial map of the product of the Hb-o and Hb-r regression slopes was generated. For presentation clarity, we show only those

contour levels that comprise the highest 90% of the computed values (*i.e.*, background contrast is <10% of the maximum value shown. Comparison of this result to the sonogram image of the same breast indicates excellent agreement. While the external boundary of the breast is not explicitly indicated in the sonogram, it is known that the tumor location indicated by the DYNOT functional image is highly accurate. The equivalent result obtained from the normal breast (not shown) yielded a spatial map that was essentially featureless within the contrast ranges shown.
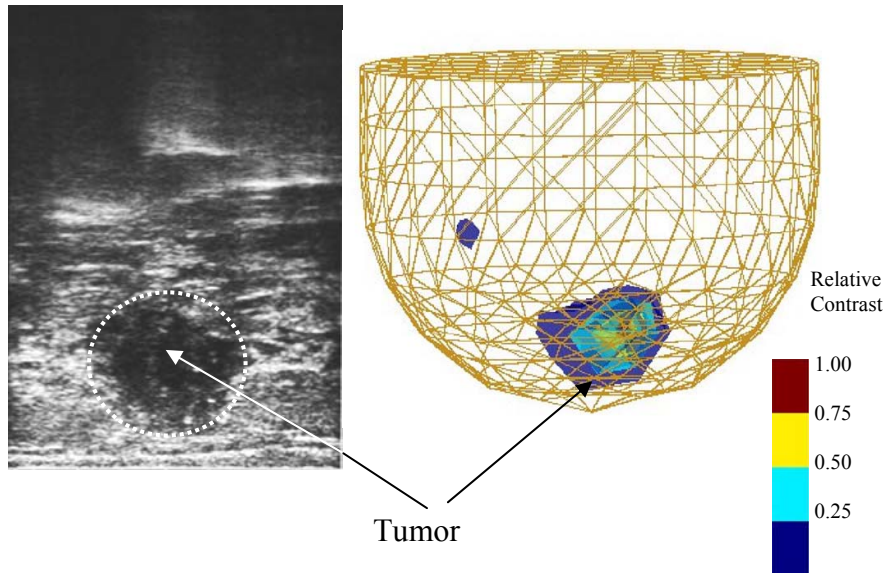
Figure 6. Right, 3D DYNOT image of tumor identifying imbalance in tissue oxygen supply/demand. Image was produced without need of contrast agents or compression. Left, sonogram image of same breast showing location of tumor. Note close agreement in size and shape.

3.3 Imaging of Temporal Heterogeneity with Principal-Component/Correlation-Coefficient Analysis

Subject III (1.5 – 2 cm diameter tumor) was asked to perform a sequence of three quantitative Valsalva maneuvers, which have well-characterized effects on blood pressure and on the rate of venous return to the heart [11]. The protocol for data collection and analysis was: 1) subject performed three cycles of quantitative Valsalva maneuver and recovery, over a period of ~9 minutes; 2) simultaneous dual-wavelength measurements were performed at a rate of ~3 Hz during this time; 3) time series of absorption coefficient (μ_a) images, at both wavelengths, were reconstructed; 4) a time series of spatial maps of Hb-o concentration was computed from the μ_a images for each time point; 5) the principal components [12] of the Hb-o time series were computed; 6) the correlations between the temporal part of the first principal component and the Hb-o time series in each image pixel were computed 7) a spatial map of the correlation coefficients computed in the preceding step was generated.

The concept underlying principal component analysis (PCA) is shown in Figure 7, where the temporal dependence of an optical coefficient or hemodynamic parameter is plotted for each pixel of a hypothetical three-pixel medium (Fig. 7(a)). While it appears that the three plotted functions are unrelated to each other, in fact each of them is simply a different linear combination of two underlying, not directly observed, time-varying functions. The truth of the preceding assertion can be seen by examining Fig. 7(b), wherein the data in the three curves of 7(a) are replotted as the three coordinates of a point moving about in a three-dimensional space. When the three-dimensional representation is rotated, it becomes apparent that the data points all lie in a single plane. That is to say, only two types of time-varying behavior are actually present in the medium.

While the graphical technique of the preceding paragraph can not be directly applied to cases in which there are more than three image pixels, the operations that constitute PCA perform the equivalent of it. If N is the number of pixels, PCA can determine whether the corresponding N time series can be represented as linear combinations of a smaller number of temporal functions. In addition, PCA will rank the underlying (or "basis") functions in order of decreasing

importance; here, importance is equated with the percentage of overall variance in the image time series that can be attributed to each basis function [12].
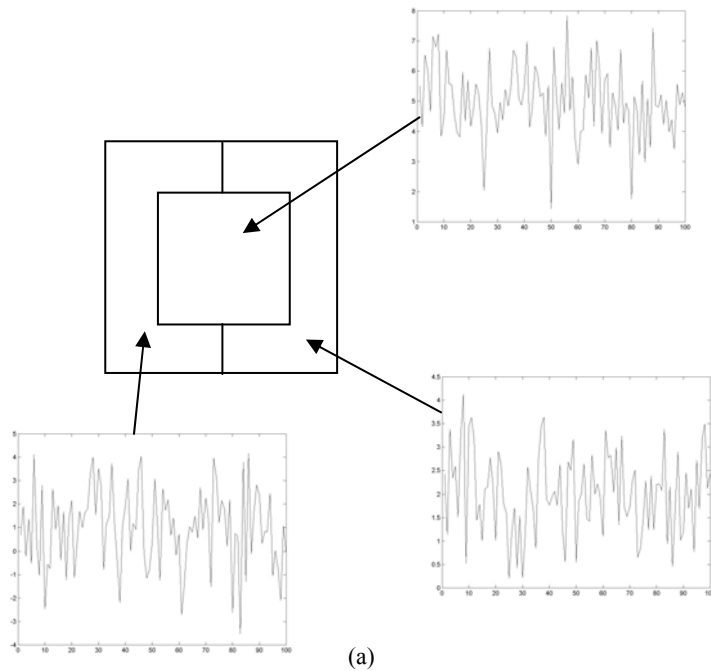

Figure 7. Sketch demonstrating the effect of performing PCA on image time series. In (a), each pixel exhibits a time-varying behavior apparently unrelated to the those of the other two. However, in (b) the three pixels' data are plotted as the three coordinates of points in 3D space, and by viewing the resulting scatterplot from different perspectives it can be seen that only two types of time-varying behavior actually are present. Each pixel's time series is a linear combination of the two.

(a)

(b)
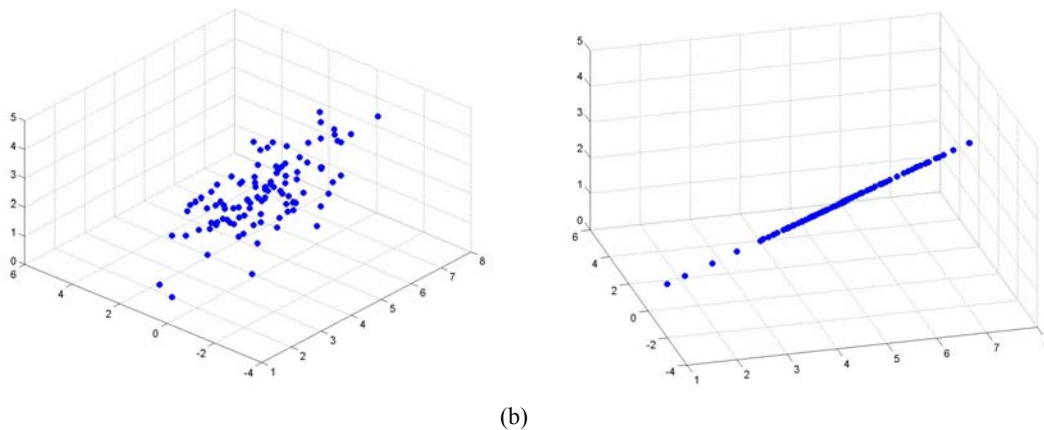
The correlations computed in step 6 of the analysis protocol is the linear correlation coefficient well known from statistics. A straightforward index of the similarity between two functions, this coefficient has a value of ±1 if the behavior of each perfectly mirrors that of the other, and is 0 if there is no simple linear relation between them.

In Figure 8 we show the results derived by applying the outlined protocol to the Hb-o image time series of the tumor-bearing breast (8(a) and 8(b)) and healthy breast (8(c) and 8(d)) of Subject III. The data points plotted in 8(a) and 8(c) show the cumulative importance of the first n principal components, $n = 1,2,…,50$. A significant difference between the tumor-bearing and healthy breasts is that the first principal component (PC) of the former accounts for less than half the overall variance in its image time series, while the first PC of the latter accounts for more than 95% of the overall variance there. The corresponding spatial maps (in which three-dimensional volumetric images such as those in Figs. 4 and 6 are reduced to two dimensions by integrating over the ventral-dorsal direction) are spatial maps of the correlation between the first PC and the Hb-o time series in each pixel. The pattern seen in 8(b) shows that in the tumor-bearing breast the largest region wherein the first PC is strongly correlated with the Hb-o time series corresponds well to the

known location of the tumor. On the other hand, no such localization is seen in the spatial map in 8(d), which is derived from the healthy-breast data. A second interesting observation, consistent with known disruptions of coordination of vascular structure and function by tumors, is that the map in 8(b) exhibits a wide range of correlation values, while most of the correlations in 8(d) lie in two clusters, suggestive of the two principal tissue types in a healthy breast, about values of +1 and 0.
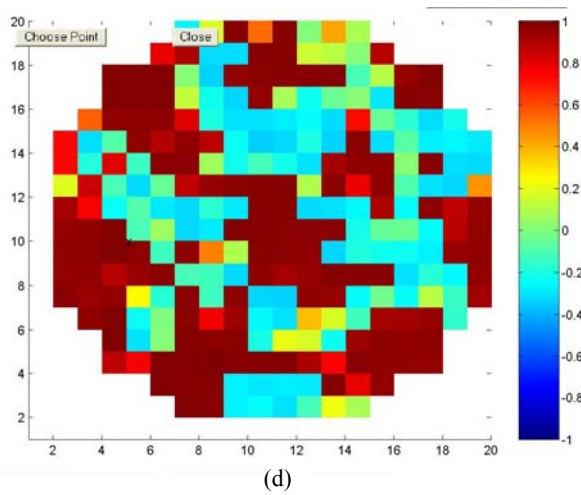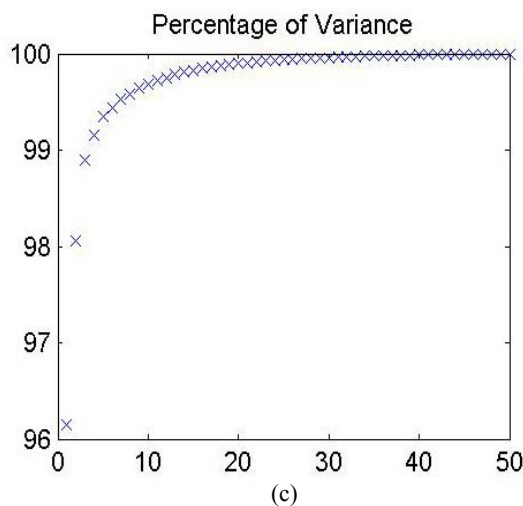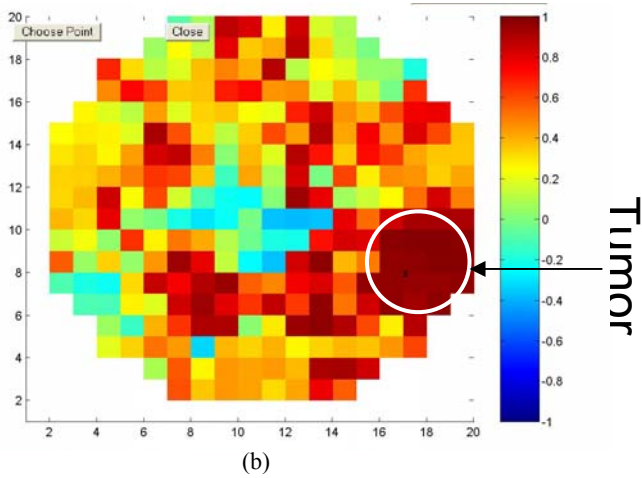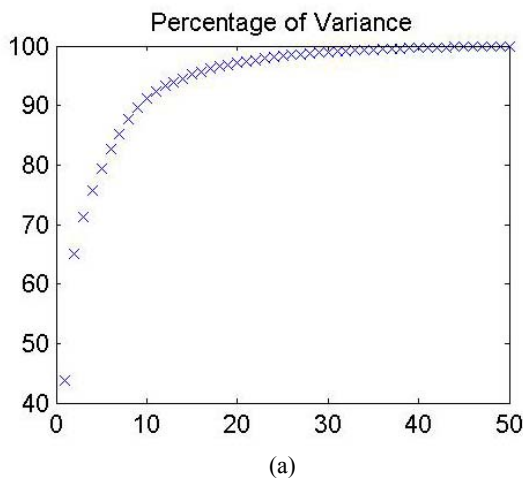
lts from application of PCA + correlation analysis to Hb-o image time series derived from measurements performed on Subject III.   In (a) the cumulative percentage of total variance in the tumor-bearing breast images accounted for by the first n PCs, $n = 1,2,\ldots,50$, is graphed. (b) shows a two-dimensional spatial map, for the tumor-bearing breast of the correlation between the first PC and the Hb-o time series in each pixel. In (c) and (d) the corresponding results for the contralateral normal breast are shown.

3.4 Imaging Altered Modulation of Vascular Rhythms with Wavelet Analysis

No respiratory or other provocations were performed in the case of Subject IV (1.5 – 2 cm diameter tumor). Instead, the protocol for data collection and analysis was: 1) simultaneous dual-wavelength measurements were performed at a rate of ~3 Hz over a period of twenty minutes, while the subject was at rest (baseline measurement protocol); 2) for each source-detector channel, time series of average tissue μ_a at both wavelengths were estimated, by means of modified Beer-Lambert law computations; 3) for each channel, a time series of average tissue Hb-t concentration was computed from that channel's μ_a data; 4) amplitude-vs.-time functions were computed for each channel's Hb-t time series, for selected "carrier" frequencies between 0 and 0.5 Hz, by means of a continuous Morlet wavelet analysis; 5) the preceding result was subjected to straightforward Fourier analysis, to determine whether there were *modulation* frequencies of particular importance within the time-varying amplitude at any of the carrier frequencies.

The concept underlying the wavelet analysis performed in step 4 above is illustrated in Figure 9. The wavelet shown in Fig. 9(a) (the product of a Gaussian function and a complex sinusoid) is positioned at the beginning of the hypothetical measured signal shown in Fig. 9(b), and the (complex) covariance between the wavelet and measured signal is computed. The wavelet is then translated one step along the time axis, and the covariance computation is repeated. Proceeding in this way, a covariance vs. time function is built up. A plot of covariance amplitude against time reveals whether the particular frequency corresponding to the indicated wavelet was present with constant amplitude throughout the entire measurement period. The corresponding results for different frequencies are obtained by stretching or compressing the wavelet, as indicated in Fig. 9(c).
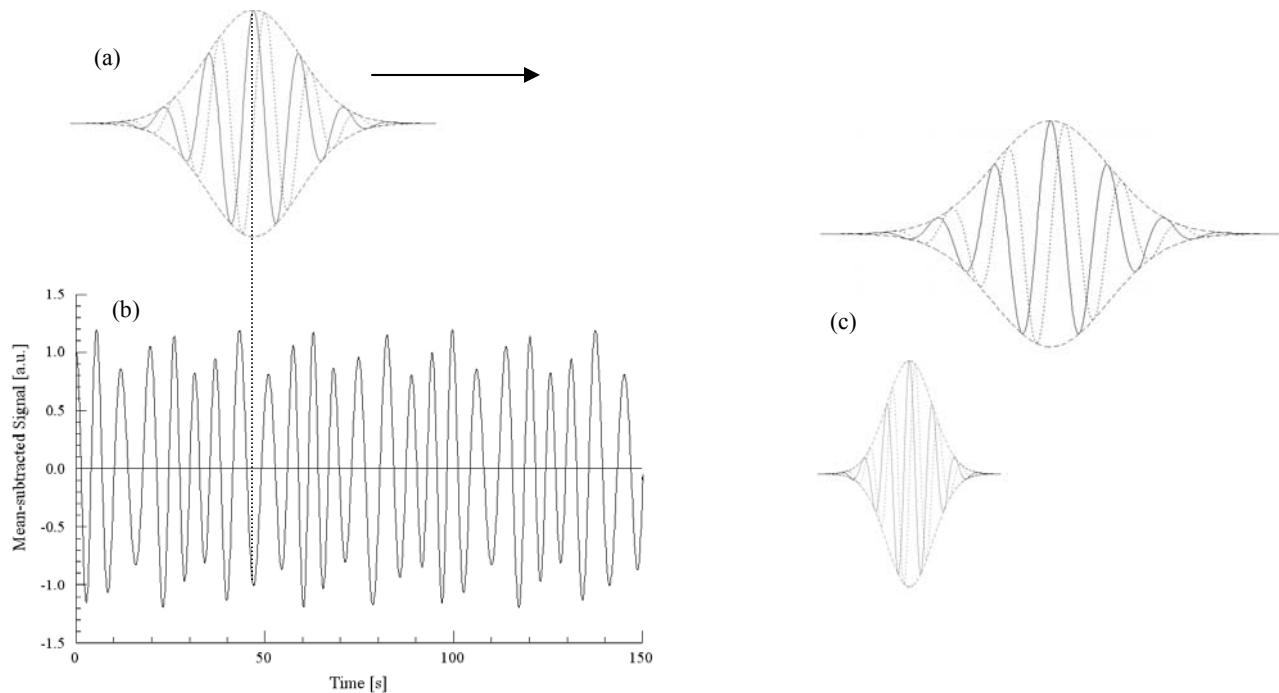
Figure 9. Illustration of Morlet wavelet analysis concept. The complex wavelet (solid and dashed sinusoidal curves denote real and imaginary part, respectively) shown in 9(a) is superimposed on the time-varying measurement depicted in 9(b). A new function, equivalent to the covariance between the wavelet and measured signal, as a function of the time point about which the wavelet is centered, is generated. (See Figure 10 for an example of such a computation.) Varying the width of the wavelet, as shown in 9(c), changes the frequency whose time-varying amplitude is computed.

A simple example of the application of the wavelet transform is shown in Figure 10. The functions used as simulated measurement data were a simple sine wave with frequency 0.1 Hz, and a frequency-modulated sine wave whose carrier and modulation frequencies were 0.1 Hz and 0.01 Hz, respectively. Each was processed, as described in the preceding paragraph, with wavelets whose widths correspond to carrier frequencies in the range 0.07 Hz to 0.13 Hz. The resulting amplitude vs. carrier frequency vs. time surface for the unmodulated sine wave is shown in Fig. 10(a), and that for the frequency-modulated wave in Fig. 10(b). The former result shows that the first signal possessed a single frequency with unvarying amplitude. The latter, on the other hand, shows that the amplitude of the second signal was fixed but its frequency was not, oscillating among values smaller and larger than 0.1 Hz over time. Note also that the modulation frequency could be determined by performing Fourier analysis of the amplitude vs. time curve corresponding to a selected carrier frequency.

Application of the protocol outlined above to the baseline measurement data obtained from Subject IV produced the result shown in Figure 11. Here, for a selected source-detector channel, we have produced a log-linear plot of the FT amplitude at a fixed modulation frequency (0.04 Hz) vs. carrier frequency. Here the curves for both the tumor-bearing (solid curve) and healthy (dashed curve) breasts are plotted together. Because the measurements on left and right breasts were not obtained at the same time, the more subtle differences between the two curves can not be accepted as significant. The ~100-fold difference in modulation amplitude seen in the 0.05-0.08 Hz carrier-frequency band
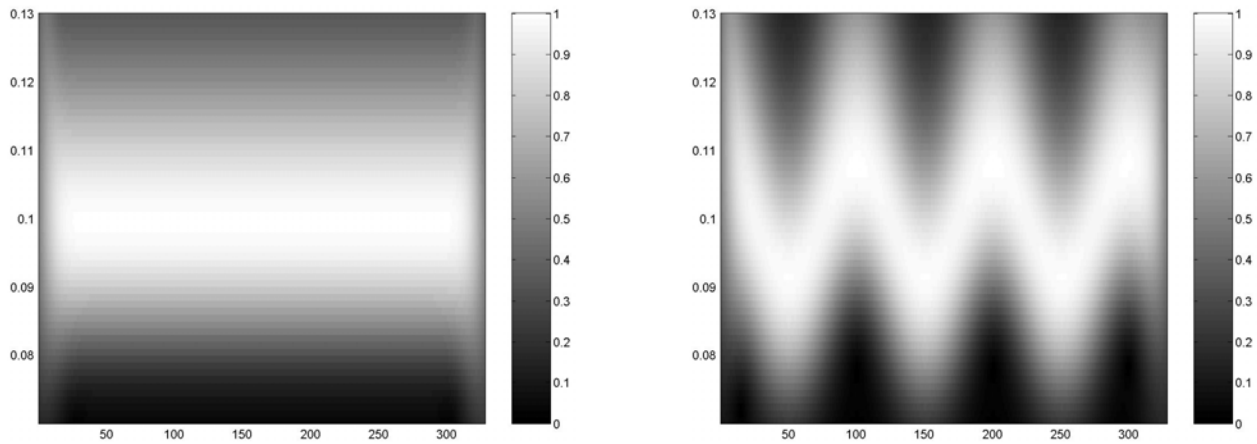
Figure 10. Result of wavelet analysis (see Fig. 9) applied to (a) an unmodulated 0.1-Hz sine wave and (b) a frequency-modulated 0.1-Hz sine wave. In 10(a) it is seen that the amplitude and frequency both are constant over time, while in 10(b) it is seen that the amplitude is fixed but the frequency varies.

(qualitatively similar results, not shown, were found in analogous studies on baseline data from the other subjects) is more probably real, however. Consequently, we have directly reconstructed images of the 0.04-Hz component of the 0.06-Hz carrier frequency's FT (dashed vertical line in Fig. 11), and recombined the real and imaginary parts of the
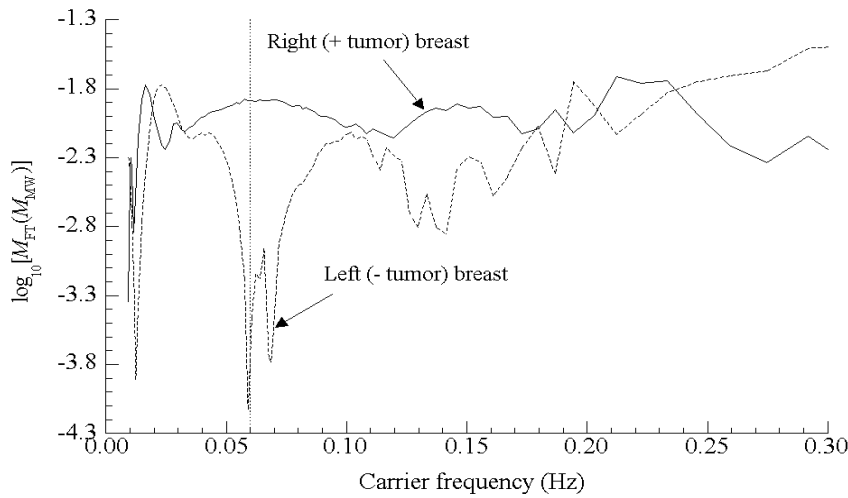
of the 0.04-Hz component of a source-detector channel's Hb-t concentration time series, vs. carrier frequency, for both the tumor-bearing and unaffected breasts of Subject IV.

result into spatial maps of the modulation amplitude. The results, for both breasts, are shown in Figure 12. When both maps are viewed on the same scale, a fairly localized region of heightened amplitude appears in the tumor-bearing breast image. It is seen that the location of this region agrees fairly well with the location of the tumor, which is known from ultrasound scans (not shown) and physical examination. The high-amplitude region extends over a larger region than the physical margins of the tumor. It should be noted that this is not necessarily an observation regarding the spatial resolution of our procedure, but might be an accurate result. It is entirely reasonable to expect that the tumor can affect the vasculature within the healthy tissue in its vicinity, and additional studies will have to be performed to determine whether that is what we are seeing in Fig. 12.
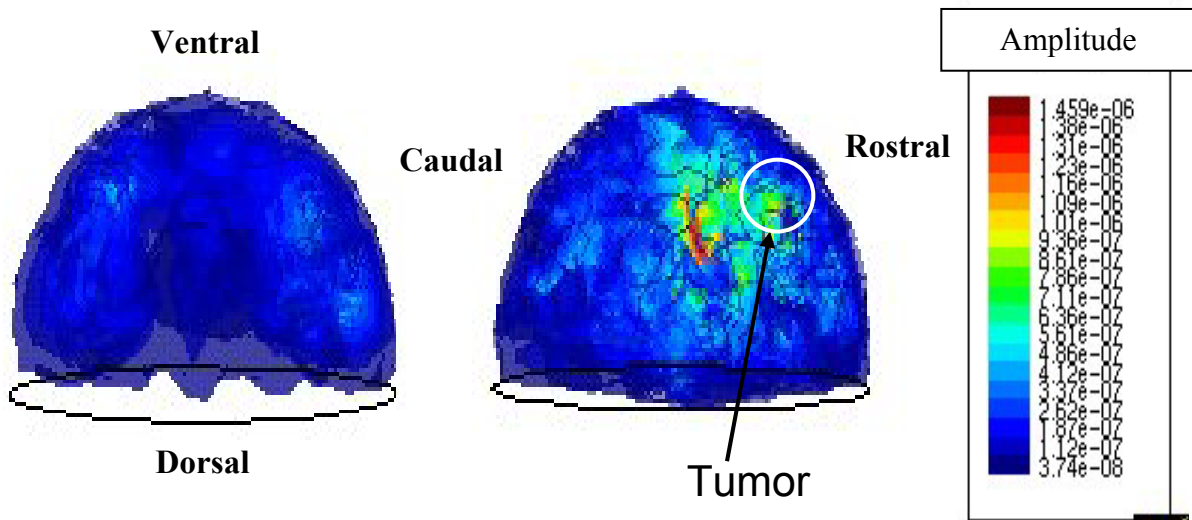
Figure 12. Spatial maps of modulation amplitude for the 0.06-Hz carrier frequency, 0.04-Hz modulation frequency combination. Shown are the results for the unaffected breast (a) and tumor-bearing breast (b). Also indicated in 12(b) are the known location and extent of the tumor.

4. DISCUSSION

At this time the DYNOT system for DC optical tomography has been developed and refined to the point where collection of data is a straightforward, almost routine process. It is important that work on answering the question of what shall be done with the data once it has been collected not be outpaced. The type of pre- and post-reconstruction analysis one decides to do will almost certainly influence the design of experimental protocol (e.g., baseline study or provocation, and if the latter is chosen, then what kind of provocation). It is at least plausible, furthermore, that the choice of protocol can reflect back onto issues of hardware design. In the current report we have shown several examples of successful application of different data-analysis strategies to optical tomographic measurements taken from breast cancer patients. In each case the techniques employed correctly distinguished the tumor-bearing breast from the contralateral unaffected breast, "diagnosed" the presence of a tumor, and identified its location with acceptable accuracy.

We do not seek to obscure the fact that all subjects considered here were in an advanced stage of already-diagnosed breast cancer, with tumors of significant size (>1 cm diameter in all cases). The cases here reported on are part of a study designed to test the DYNOT system's ability to monitor patient response to neoadjuvant chemotheraphy. As such, it could have an important function in breast cancer clinics. We have not yet sought to examine the utility of the DYNOT system as a potential screening tool.

Refinements of the experimental technique that are currently in development include the construction of a dual measuring head device, for simultaneous recording from both breasts. At the same time we are exploring the use of different types of provocation, such as temperature shock, postural changes (e.g., head-up and head-down tilts), and controlled inspiration of defined gas mixtures. An important advantage that these present relative to controlled respiration is that they make fewer demands upon the subjects, some of whom can not hold their breaths for long or are not capable of performing the Valsalva maneuver. Attempts to determine the receiver operator characteristics of DYNOT for different stages of breast cancer, and to test it as a possible screening tool, will be feasible after these improvements are completed.

5. ACKNOWLEDGMENTS

6. REFERENCES

1. R. L. Barbour, H. L. Graber, Y. Pei, S. Zhong, and C. H. Schmitz, "Optical tomographic imaging of dynamic features of dense-scattering media," *J. Opt. Soc. Am. A* **18**, 3018-3036 (2001).

2. C. H. Schmitz, M. Löcker, J. M. Lasker, A. H. Hielscher, and R. L. Barbour, "Instrumentation for fast functional optical tomography," *Rev. Sci. Instrum.* 73, 429-439 (2002).

3. C. H. Schmitz, Y.Pei, H. L. Graber, J. M. Lasker, A. H. Hielscher, and R. L. Barbour, "Instrumentation for real-time dynamic optical tomography," in *Photon Migration, Optical Coherence Tomography, and Microscopy (Proceedings of SPIE, Vol. 4431)*, pp. 282-291 (2001).

4. C. H. Schmitz, H. L. Graber, H. Luo, I. Arif, J. Hira, Y. Pei, A. Bluestone, S. Zhong, R. Andronica, I. Soller, N. Ramirez, S.-L. S. Barbour, and R. L. Barbour, "Instrumentation and calibration protocol for imaging dynamic features in dense-scattering media by optical tomography," *Appl. Opt.* **39**, 6466-6486 (2000).

5. G. S. Landis, T. F. Panetta, S. B. Blattman, H. L. Graber, Y. Pei, C. H. Schmitz, and R. L. Barbour, "Clinical applications of dynamic optical tomography in vascular disease," in *Optical Tomography and Spectroscopy of Tissues IV (Proceedings of SPIE, Vol. 4250)*, pp. 130-141 (2001).

6. R. L. Barbour, H. L. Graber, Y. Pei, and C. H. Schmitz, "Imaging of vascular chaos," in *Optical Tomography and Spectroscopy of Tissues IV (Proceedings of SPIE, Vol. 4250)*, pp. 577-590 (2001).

7. R. L. Barbour, C. H. Schmitz, and H. L. Graber, "Dynamic functional imaging of the healthy and cancerous breasts by optical tomography," *OSA Biomedical Topical Meetings: Advances in Optical Imaging and Photon Migration* (Miami Beach, Fl, Apr. 7-10, 2002), pp. 456-458.

8. Y. Pei, H. L. Graber, and R. L. Barbour, "Influence of systematic errors in reference states on image quality and on stability of derived information for DC optical imaging," *Appl. Opt.* **40**, 5755-5769 (2001).

9. Y. Pei, H. L. Graber, and R. L. Barbour, "A reconstruction technique for time-series DC optical tomography," accompanying article in these proceedings.

10. M. Molls and P. Vaupel, "The impact of the tumor microenvironment on experimental and clinical radiation oncology and other therapeutic modalities," in *Blood Perfusion and Microenvironment of Human Tumors*, M. Molls and P. Vaupels, Eds. (Springer-Verlag, Berlin, 2000).

11. H. Olschewski and K. Bruck, "Cardiac responses to Valsalva manoeuvre in different body position," *Eur. J. Appl. Physiol.* **61**, 20-25 (1990).

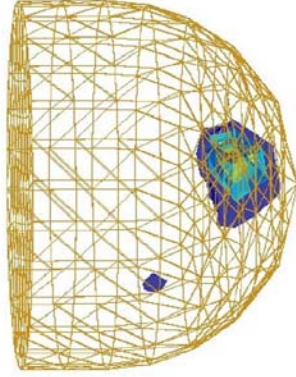12. M. Stetter, *Exploration of Cortical Function* (Kluwer Academic, Dordrecht, 2002), Chap. 7, §2.
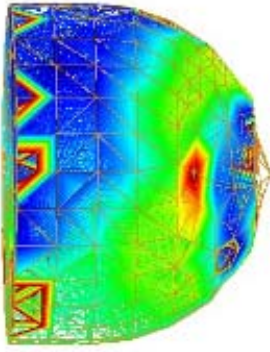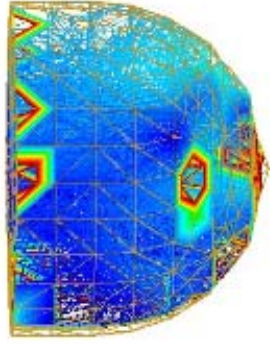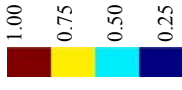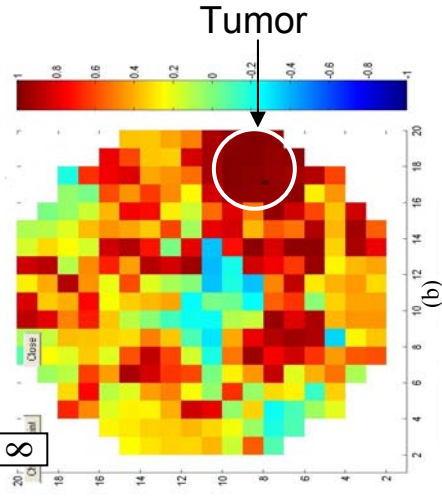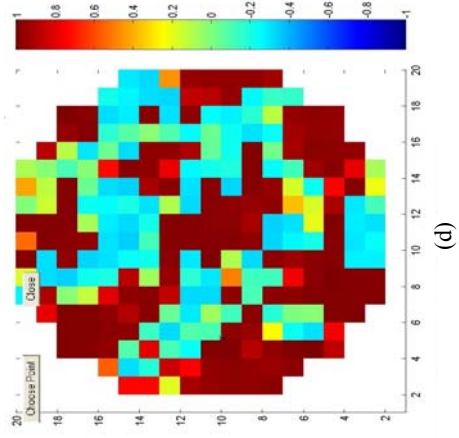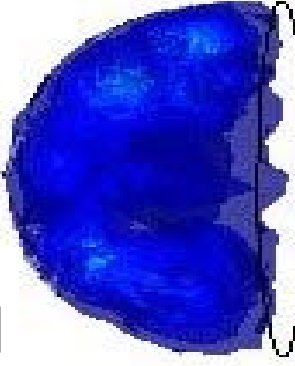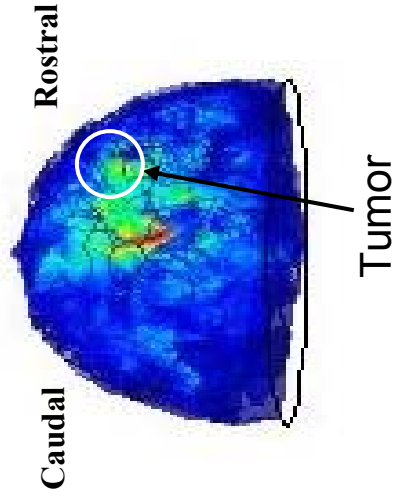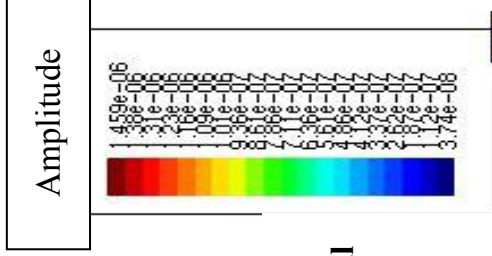
Shown here are full-color reproductions of the 2D and 3D optical feature maps in Figures 4, 6, 8, and 12.